Research Article | Vol. 25, No. 24 | 27 Nov 2017 | OPTICS EXPRESS 30732
Optics EXPRESS

Automated detection of cloud and aerosol features with SACOL micro-pulse lidar in northwest China

Hailing Xie,[1] Tian Zhou,[1,*] Qiang Fu,[1,2] Jianping Huang,[1] Zhongwei Huang,[1] Jianrong Bi,[1] Jinsen Shi,[1] Beidou Zhang,[1] and Jinming Ge[1]

[1]*Key Laboratory for Semi-Arid Climate Change of the Ministry of Education, College of Atmospheric Sciences, Lanzhou University, Lanzhou, 730000, China*
[2]*Department of Atmospheric Sciences, University of Washington, Seattle, WA, 898105, USA*
**zhoutian@lzu.edu.cn*

Abstract: The detection of cloud and aerosols using a modified retrieval algorithm solely for a ground-based micropulse lidar (MPL) is presented, based on one-year data at the Semi-Arid Climate Observatory and Laboratory (SACOL) site (35.57°N, 104.08°E, 1965.8 m), northwest of China, from March 2011 to February 2012. The work not only identifies atmosphere particle layers by means of the range-dependent thresholds based on elastic scattering ratio and depolarization ratio, but also discriminates the detected layers by combining empirical thresholds of the atmosphere's thermodynamics states and scattering properties and continuous wavelet transform (CWT) analyses. Two cases were first presented in detail that demonstrated that the modified algorithm can capture atmosphere layers well. The cloud macro-physical properties including cloud base height (CBH), cloud geometrical thickness (CGT), and cloud fraction (CF) were then analyzed in terms of their monthly and seasonal variations. It is shown that the maximum/minimum CBHs were found in summer (4.66 ± 1.95km)/autumn (3.34 ± 1.84km). The CGT in winter (1.05 ± 0.43km) is slightly greater than in summer (0.99 ± 0.44km). CF varies significantly throughout year, with the maximum value in autumn (0.68), and a minimum (0.58) in winter, which is dominated by single-layered clouds (81%). The vertical distribution of CF shows a bimodal distribution, with a lower peak between 1 and 4km and a higher one between 6and 9km. The seasonal and vertical variations in CF are important for the local radiative energy budget.

OCIS codes: (010.1615) Clouds; (010.1100) Aerosol detection; (010.1110) Aerosols; (010.3640) Lidar; (280.0280) Remote sensing and sensors; (290.0290) Scattering.

References and links

1. Q. Fu, "A new parameterization of an asymmetry factor of cirrus clouds for climate models," J. Atmos. Sci. **64**(11), 4140–4150 (2007).
2. Q. Fu, M. Baker, and D. L. Hartmann, "Tropical cirrus and water vapor: an effective Earth infrared iris feedback?" Atmos. Chem. Phys. **2**(1), 31–37 (2002).
3. J. Huang, Q. Fu, J. Su, Q. Tang, P. Minnis, Y. Hu, Y. Yi, and Q. Zhao, "Taklimakan dust aerosol radiative heating derived from CALIPSO observations using the Fu-Liou radiation model with CERES constraints," Atmos. Chem. Phys. **9**(12), 4011–4021 (2009).
4. J. P. Huang, B. Lin, P. Minnis, T. H. Wang, X. Wang, Y. X. Hu, Y. H. Yi, and J. K. Ayers, "Satellite-based assessment of possible dust aerosols semi-direct effect on cloud water path over East Asia," Geophys. Res. Lett. **33**(19), L19802 (2006b).
5. J. P. Huang, P. Minnis, B. Lin, T. H. Wang, Y. H. Yi, Y. X. Hu, S. Sun-Mack, and K. Ayers, "Possible influences of Asian dust aerosols on cloud properties and radiative forcing observed from MODIS and CERES," Geophys. Res. Lett. **33**(6), L06824 (2006).
6. U. Lohmann and B. Gasparini, "A cirrus cloud climate dial?" Science **357**(6348), 248–249 (2017).
7. G. L. Stephens, J. L. Li, M. Wild, C. A. Clayson, N. Loeb, S. Kato, T. L'Ecuyer, P. W. Stackhouse, M. Lebsock, and T. Andrews, "An update on Earth's energy balance in light of the latest global observations," Nat. Geosci. **5**(10), 691–696 (2012).

#307252 https://doi.org/10.1364/OE.25.030732
Journal © 2017 Received 15 Sep 2017; revised 28 Oct 2017; accepted 31 Oct 2017; published 22 Nov 2017
Corrected: 08 December 2017

Optics EXPRESS

8. J. Su, J. P. Huang, Q. Fu, P. Minnis, J. M. Ge, and J. R. Bi, "Estimation of Asian dust aerosol effect on cloud radiation forcing using Fu-Liou radiative model and CERES measurements," Atmos. Chem. Phys. **8**(10), 2763–2771 (2008).
9. T. J. Thorsen, Q. Fu, and J. M. Comstock, "Cloud effects on radiative heating rate profiles over Darwin using ARM and A-train radar/lidar observations," J. Geophys. Res. Atmos. **118**(11), 5637–5654 (2013b).
10. T. J. Garrett and C. Zhao, "Ground-based remote sensing of thin clouds in the Arctic," Atmos. Meas. Tech. **6**(5), 1227–1243 (2013).
11. C. F. Zhao and T. J. Garrett, "Effects of Arctic haze on surface cloud radiative forcing," Geophys. Res. Lett. **42**(2), 557–564 (2015).
12. T. J. Garrett and C. Zhao, "Increased Arctic cloud longwave emissivity associated with pollution from mid-latitudes," Nature **440**(7085), 787–789 (2006).
13. Q. Bourgeois, A. M. L. Ekman, M. R. Igel, and R. Krejci, "Ubiquity and impact of thin mid-level clouds in the tropics," Nat. Commun. **7**, 12432 (2016).
14. G. L. Stephens, "Cloud feedbacks in the climate system: A critical review," J. Clim. **18**(2), 237–273 (2005).
15. T. F. Stocker, D. Qin, G. K. Plattner, L. V. Alexander, S. K. Allen, N. L. Bindoff, F. M. Bréon, J. A. Church, U. Cubasch, and S. Emori, IPCC: Technical Summary. In: Climate Change 2013: The Physical Science Basis. Contribution of Working Group I to the Fifth Assessment Report of the Intergovernmental Panel on Climate Change (Cambridge University, 2013).
16. S. C. Xie, X. H. Liu, C. F. Zhao, and Y. Y. Zhang, "Sensitivity of CAM5-Simulated Arctic Clouds and Radiation to Ice Nucleation Parameterization," J. Clim. **26**(16), 5981–5999 (2013).
17. Q. Fu, M. C. Cribb, H. W. Barker, S. K. Krueger, and A. Grossman, "Cloud geometry effects on atmospheric solar absorption," J. Atmos. Sci. **57**(8), 1156–1168 (2000).
18. Q. Fu, B. Carlin, and G. Mace, "Cirrus horizontal inhomogeneity and OLR bias," Geophys. Res. Lett. **27**(20), 3341–3344 (2000).
19. K. N. Liou, An introduction to atmospheric radiation (Academic, 2002).
20. B. Carlin, Q. Fu, U. Lohmann, G. G. Mace, K. Sassen, and J. M. Comstock, "High-cloud horizontal inhomogeneity and solar albedo bias," J. Clim. **15**(17), 2321–2339 (2002).
21. Z. Wang, G. M. Heymsfield, L. H. Li, and A. J. Heymsfield, "Retrieving optically thick ice cloud microphysical properties by using airborne dual-wavelength radar measurements," J. Geophys. Res. Atmos. **110**(D19), D19201 (2005).
22. S. Fueglistaler and Q. Fu, "Impact of clouds on radiative heating rates in the tropical lower stratosphere," J. Geophys. Res. Atmos. **111**(D23), n/a (2006).
23. Q. Fu, Y. Hu, and Q. Yang, "Identifying the top of the tropical tropopause layer from vertical mass flux analysis and CALIPSO lidar cloud observations," Geophys. Res. Lett. **34**, L14813 (2007).
24. Q. Yang, Q. Fu, and Y. X. Hu, "Radiative impacts of clouds in the tropical tropopause layer," J. Geophys. Res. Atmos. **115**, D00H12 (2010).
25. X. Q. Dong, B. K. Xi, A. Kennedy, P. Minnis, and R. Wood, "A 19-Month Record of Marine Aerosol- Cloud-Radiation Properties Derived from DOE ARM Mobile Facility Deployment at the Azores. Part I: Cloud Fraction and Single-Layered MBL Cloud Properties," J. Clim. **27**(10), 3665–3682 (2014).
26. J. R. Campbell, S. Lolli, J. R. Lewis, Y. Gu, and E. J. Welton, "Daytime Cirrus Cloud Top-of-the-Atmosphere Radiative Forcing Properties at a Midlatitude Site and Their Global Consequences," J. Appl. Meteorol. Climatol. **55**(8), 1667–1679 (2016).
27. C. F. Zhao, L. P. Liu, Q. Q. Wang, Y. M. Qiu, Y. Wang, and X. L. Wu, "MMCR-based characteristic properties of non-precipitating cloud liquid droplets at Naqu site over Tibetan Plateau in July 2014," Atmos. Res. **190**, 68–76 (2017).
28. C. F. Zhao, S. C. Xie, S. A. Klein, A. Protat, M. D. Shupe, S. A. McFarlane, J. M. Comstock, J. Delanoe, M. Deng, M. Dunn, R. J. Hogan, D. Huang, M. P. Jensen, G. G. Mace, R. McCoy, E. J. O'Connor, D. D. Turner, and Z. Wang, "Toward understanding of differences in current cloud retrievals of ARM ground-based measurements," J. Geophys. Res. Atmos. **117**, D10206 (2012).
29. C. J. Stubenrauch, W. B. Rossow, S. Kinne, S. Ackerman, G. Cesana, H. Chepfer, L. Di Girolamo, B. Getzewich, A. Guignard, A. Heidinger, B. C. Maddux, W. P. Menzel, P. Minnis, C. Pearl, S. Platnick, C. Poulsen, J. Riedi, S. Sun-Mack, A. Walther, D. Winker, S. Zeng, and G. Zhao, "Assessment of Global Cloud Datasets from Satellites: Project and Database Initiated by the GEWEX Radiation Panel," Bull. Am. Meteorol. Soc. **94**(7), 1031–1049 (2013).
30. D. Huang, C. Zhao, M. Dunn, X. Dong, G. G. Mace, M. P. Jensen, S. Xie, and Y. Liu, "An intercomparison of radar-based liquid cloud microphysics retrievals and implications for model evaluation studies," Atmos. Meas. Tech. **5**(6), 1409–1424 (2012).
31. D. D. Turner and U. Lohnert, "Information Content and Uncertainties in Thermodynamic Profiles and Liquid Cloud Properties Retrieved from the Ground-Based Atmospheric Emitted Radiance Interferometer (AERI)," J. Appl. Meteorol. Climatol. **53**(3), 752–771 (2014).
32. C. F. Zhao, S. C. Xie, X. Chen, M. P. Jensen, and M. Dunn, "Quantifying uncertainties of cloud microphysical property retrievals with a perturbation method," J. Geophys. Res. Atmos. **119**(9), 5375–5385 (2014a).
33. S. A. Ackerman, R. E. Holz, R. Frey, E. W. Eloranta, B. C. Maddux, and M. McGill, "Cloud detection with MODIS. Part II: Validation," J. Atmos. Ocean. Technol. **25**(7), 1073–1086 (2008).

Optics EXPRESS

34. J. P. Huang, P. Minnis, B. Lin, Y. H. Yi, M. M. Khaiyer, R. F. Arduini, A. Fan, and G. G. Mace, "Advanced retrievals of multilayered cloud properties using multispectral measurements," J. Geophys. Res. Atmos. **110**(D15), D15S18 (2005).
35. F. L. Chang and Z. Q. Li, "A new method for detection of cirrus overlapping water clouds and determination of their optical properties," J. Atmos. Sci. **62**(11), 3993–4009 (2005).
36. Z. Wang and K. Sassen, "Cirrus cloud microphysical property retrieval using lidar and radar measurements. Part II: Midlatitude cirrus microphysical and radiative properties," J. Atmos. Sci. **59**(14), 2291–2302 (2002b).
37. Z. Wang and K. Sassen, "Cirrus cloud microphysical property retrieval using lidar and radar measurements. Part I: Algorithm description and comparison with in situ data," J. Appl. Meteorol. **41**(3), 218–229 (2002a).
38. D. M. Winker, J. Pelon, J. A. Coakley, Jr., S. A. Ackerman, R. J. Charlson, P. R. Colarco, P. Flamant, Q. Fu, R. M. Hoff, C. Kittaka, T. L. Kubar, H. Le Treut, M. P. Mccormick, G. Mégie, L. Poole, K. Powell, C. Trepte, M. A. Vaughan, and B. A. Wielicki, "The CALIPSO Mission," Bull. Am. Meteorol. Soc. **91**(9), 1211–1230 (2010).
39. A. J. Illingworth, H. W. Barker, A. Beljaars, M. Ceccaldi, H. Chepfer, N. Clerbaux, J. Cole, J. Delanoe, C. Domenech, D. P. Donovan, S. Fukuda, M. Hirakata, R. J. Hogan, A. Huenerbein, P. Kollias, T. Kubota, T. Nakajima, T. Y. Nakajima, T. Nishizawa, Y. Ohno, H. Okamoto, R. Oki, K. Sato, M. Satoh, M. W. Shephard, A. Velazquez-Blazquez, U. Wandinger, T. Wehr, and G.-J. van Zadelhoff, "THE EARTHCARE SATELLITE The Next Step Forward in Global Measurements of Clouds, Aerosols, Precipitation, and Radiation," Bull. Am. Meteorol. Soc. **96**(8), 1311–1332 (2015).
40. J. M. Li, Q. Y. Lv, M. Zhang, T. H. Wang, K. Kawamoto, S. Y. Chen, and B. D. Zhang, "Effects of atmospheric dynamics and aerosols on the fraction of supercooled water clouds," Atmos. Chem. Phys. **17**(3), 1847–1863 (2017).
41. T. Luo, Z. Wang, D. M. Zhang, and B. Chen, "Marine boundary layer structure as observed by A-train satellites," Atmos. Chem. Phys. **16**(9), 5891–5903 (2016).
42. T. M. Chen, J. P. Guo, Z. Q. Li, C. F. Zhao, H. Liu, M. Cribb, F. Wang, and J. He, "A CloudSat Perspective on the Cloud Climatology and Its Association with Aerosol Perturbations in the Vertical over Eastern China," J. Atmos. Sci. **73**(9), 3599–3616 (2016).
43. J. R. Lewis, J. R. Campbell, E. J. Welton, S. A. Stewart, and P. C. Haftings, "Overview of MPLNET, Version 3, Cloud Detection," J. Atmos. Ocean. Technol. **33**(10), 2113–2134 (2016).
44. Z. Wang and K. Sassen, "Cloud type and macrophysical property retrieval using multiple remote sensors," J. Appl. Meteorol. **40**(10), 1665–1682 (2001).
45. J. P. Huang, J. J. Liu, B. Chen, and S. L. Nasiri, "Detection of anthropogenic dust using CALIPSO lidar measurements," Atmos. Chem. Phys. **15**(20), 11653–11665 (2015).
46. H. Baars, P. Seifert, R. Engelmann, and U. Wandinger, "Target categorization of aerosol and clouds by continuous multiwavelength-polarization lidar measurements," Atmos. Meas. Tech. **10**(9), 3175–3201 (2017).
47. S. R. Pal, W. Steinbrecht, and A. I. Carswell, "Automated method for lidar determination of cloud-base height and vertical extent," Appl. Opt. **31**(10), 1488–1494 (1992).
48. K. Sassen and B. S. Cho, "Subvisual Thin Cirrus Lidar Dataset for Satellite Verification and Climatological Research," J. Appl. Meteorol. **31**(11), 1275–1285 (1992).
49. D. M. Winker and M. A. Vaughan, "Vertical distribution of clouds over Hampton, Virginia observed by lidar under the ECLIPS and FIRE ETO programs," Atmos. Res. **34**(1-4), 117–133 (1994).
50. J. R. Campbell, K. Sassen, and E. J. Welton, "Elevated cloud and aerosol layer retrievals from Micropulse Lidar Signal Profiles," J. Atmos. Ocean. Technol. **25**(5), 685–700 (2008).
51. M. A. Vaughan, K. A. Powell, D. M. Winker, C. A. Hostetler, R. E. Kuehn, W. H. Hunt, B. J. Getzewich, S. A. Young, Z. Liu, and M. J. McGill, "Fully Automated Detection of Cloud and Aerosol Layers in the CALIPSO Lidar Measurements," J. Atmos. Ocean. Technol. **26**(10), 2034–2050 (2009).
52. I. M. Brooks, "Finding boundary layer top: Application of a wavelet covariance transform to lidar backscatter profiles," J. Atmos. Ocean. Technol. **20**(8), 1092–1105 (2003).
53. S. A. Cohn and W. M. Angevine, "Boundary layer height and entrainment zone thickness measured by lidars and wind-profiling radars," J. Appl. Meteorol. **39**(8), 1233–1247 (2000).
54. Y. Morille, M. Haeffelin, P. Drobinski, and J. Pelon, "STRAT: An automated algorithm to retrieve the vertical structure of the atmosphere from single-channel lidar data," J. Atmos. Ocean. Technol. **24**(5), 761–775 (2007).
55. C. F. Zhao, Y. Z. Wang, Q. Q. Wang, Z. Q. Li, Z. E. Wang, and D. Liu, "A new cloud and aerosol layer detection method based on micropulse lidar measurements," J. Geophys. Res. Atmos. **119**(11), 6788–6802 (2014b).
56. J. J. Liu, Z. Q. Li, Y. F. Zheng, and M. Cribb, "Cloud-base distribution and cirrus properties based on micropulse lidar measurements at a site in southeastern China," Adv. Atmos. Sci. **32**(7), 991–1004 (2015).
57. T. J. Thorsen, Q. Fu, R. K. Newsom, D. D. Turner, and J. M. Comstock, "Automated Retrieval of Cloud and Aerosol Properties from the ARM Raman Lidar. Part I: Feature Detection," J. Atmos. Ocean. Technol. **32**(11), 1977–1998 (2015a).
58. T. J. Thorsen and Q. Fu, "Automated Retrieval of Cloud and Aerosol Properties from the ARM Raman Lidar. Part II: Extinction," J. Atmos. Ocean. Technol. **32**(11), 1999–2023 (2015b).
59. Z. W. Huang, J. P. Huang, J. R. Bi, G. Y. Wang, W. C. Wang, Q. A. Fu, Z. Q. Li, S. C. Tsay, and J. S. Shi, "Dust aerosol vertical structure measurements using three MPL lidars during 2008 China-US joint dust field experiment," J. Geophys. Res. Atmos. **115**, D00K15 (2010).

Optics EXPRESS

60. W. C. Wang, J. P. Huang, T. Zhou, J. R. Bi, L. Lin, Y. H. Chen, Z. W. Huang, and J. Su, "Estimation of radiative effect of a heavy dust storm over northwest China using Fu-Liou model and ground measurements," J. Quant. Spectrosc. Ra. **122**, 114–126 (2013).
61. J. Huang, W. Zhang, J. Zuo, J. Bi, J. Shi, X. Wang, Z. Chang, Z. Huang, S. Yang, B. Zhang, G. Wang, G. Feng, J. Yuan, L. Zhang, H. Zuo, S. Wang, C. Fu, and C. Jifan, "An Overview of the Semi-arid Climate and Environment Research Observatory over the Loess Plateau," Adv. Atmos. Sci. **25**(6), 906–921 (2008).
62. Y. Liu, J. Huang, G. Shi, T. Takamura, P. Khatri, J. Bi, J. Shi, T. Wang, X. Wang, and B. Zhang, "Aerosol optical properties and radiative effect determined from sky-radiometer over Loess Plateau of Northwest China," Atmos. Chem. Phys. **11**(22), 11455–11463 (2011).
63. J. M. Ge, Z. E. Zhu, C. Zheng, H. L. Xie, T. Zhou, J. P. Huang, and Q. Fu, "An improved hydrometeor detection method for millimeter-wavelength cloud radar," Atmos. Chem. Phys. **17**(14), 9035–9047 (2017).
64. E. J. Welton, J. R. Campbell, J. D. Spinhirne, and V. S. Scott III, "Global monitoring of clouds and aerosols using a network of micro-pulse lidar systems," Lidar Remote Sensing for Industry and Environment Monitoring **4153**, 151–158 (2001).
65. J. R. Campbell, D. L. Hlavka, E. J. Welton, C. J. Flynn, D. D. Turner, J. D. Spinhirne, V. S. Scott III, and I. H. Hwang, "Full-time, eye-safe cloud and aerosol lidar observation at atmospheric radiation measurement program sites: Instruments and data processing," J. Atmos. Ocean. Technol. **19**(4), 431–442 (2002).
66. E. J. Welton and J. R. Campbell, "Micropulse lidar signals: Uncertainty analysis," J. Atmos. Ocean. Technol. **19**(12), 2089–2094 (2002).
67. D. P. Dee, S. M. Uppala, A. J. Simmons, P. Berrisford, P. Poli, S. Kobayashi, U. Andrae, M. A. Balmaseda, G. Balsamo, P. Bauer, P. Bechtold, A. C. M. Beljaars, L. van de Berg, J. Bidlot, N. Bormann, C. Delsol, R. Dragani, M. Fuentes, A. J. Geer, L. Haimberger, S. B. Healy, H. Hersbach, E. V. Holm, L. Isaksen, P. Kallberg, M. Kohler, M. Matricardi, A. P. McNally, B. M. Monge-Sanz, J. J. Morcrette, B. K. Park, C. Peubey, P. de Rosnay, C. Tavolato, J. N. Thepaut, and F. Vitart, "The ERA-Interim reanalysis: configuration and performance of the data assimilation system," Q. J. R. Meteorol. Soc. **137**(656), 553–597 (2011).
68. R. H. Kingston, *Detection of Optical and Infrared Radiation* (Springer-Verlag, 1978).
69. R. M. Measures, *Laser Remote Sensing: Fundamentals and Applications* (Wiley, 1984).
70. C. J. Flynn, A. Mendoza, Y. Zheng, and S. Mathur, "Novel polarization-sensitive micropulse lidar measurement technique," Opt. Express **15**(6), 2785–2790 (2007).
71. A. Bucholtz, "Rayleigh-scattering calculations for the terrestrial atmosphere," Appl. Opt. **34**(15), 2765–2773 (1995).
72. S. Lolli, L. Sauvage, I. Stachlewska, R. Coulter, R. Newsom, "Assessment of EZ lidar and ARM/SGP MPL lidar performances for qualitative and quantitative measurements of aerosol and clouds," Geos. Rsch. Abstracts, 10, EGU-A-11091, (2008).
73. P. R. Bevington and D. K. Robinson, *Data Reduction and Error Analysis for the Physical Sciences. 3rd ed.* (McGraw-Hill, 2002).
74. T. J. Thorsen, Q. Fu, and J. Comstock, "Comparison of the CALIPSO satellite and ground-based observations of cirrus clouds at the ARM TWP sites," J. Geophys. Res. Atmos. **116**(D21), D21203 (2011).
75. M. D. Shupe, "A ground-based multisensor cloud phase classifier," Geophys. Res. Lett. **34**(22), L22809 (2007).
76. R. Tapakis and A. G. Charalambides, "Equipment and methodologies for cloud detection and classification: A review," Sol. Energy **95**, 392–430 (2013).
77. F. G. Fernald, "Analysis of atmospheric lidar observations: some comments," Appl. Opt. **23**(5), 652–653 (1984).
78. Z. Y. Liu, M. Vaughan, D. Winker, C. Kittaka, B. Getzewich, R. Kuehn, A. Omar, K. Powell, C. Trepte, and C. Hostetler, "The CALIPSO Lidar Cloud and Aerosol Discrimination: Version 2 Algorithm and Initial Assessment of Performance," J. Atmos. Ocean. Technol. **26**(7), 1198–1213 (2009).
79. A. H. Omar, D. M. Winker, M. A. Vaughan, Y. Hu, C. R. Trepte, R. A. Ferrare, K.-P. Lee, C. A. Hostetler, C. Kittaka, R. R. Rogers, R. E. Kuehn, and Z. Liu, "The CALIPSO Automated Aerosol Classification and Lidar Ratio Selection Algorithm," J. Atmos. Ocean. Technol. **26**(10), 1994–2014 (2009).
80. B. Chen, J. Huang, P. Minnis, Y. Hu, Y. Yi, Z. Liu, D. Zhang, and X. Wang, "Detection of dust aerosol by combining CALIPSO active lidar and passive IIR measurements," Atmos. Chem. Phys. **10**(9), 4241–4251 (2010).
81. T. Luo, Z. E. Wang, D. M. Zhang, X. H. Liu, Y. Wang, and R. M. Yuan, "Global dust distribution from improved thin dust layer detection using A-train satellite lidar observations," Geophys. Res. Lett. **42**(2), 620–628 (2015).
82. T. Zhou, J. Huang, Z. Huang, J. Liu, W. Wang, and L. Lin, "The depolarization-attenuated backscatter relationship for dust plumes," Opt. Express **21**(13), 15195–15204 (2013).
83. T. J. Thorsen, Q. Fu, J. M. Comstock, C. Sivaraman, M. A. Vaughan, D. M. Winker, and D. D. Turner, "Macrophysical properties of tropical cirrus clouds from the CALIPSO satellite and from ground-based micropulse and Raman lidars," J. Geophys. Res. Atmos. **118**(16), 9209–9220 (2013a).
84. X. Q. Dong, B. K. Xi, K. Crosby, C. N. Long, R. S. Stone, and M. D. Shupe, "A 10 year climatology of Arctic cloud fraction and radiative forcing at Barrow, Alaska," J. Geophys. Res. Atmos. **115**(D17), D17212 (2010).
85. X. Q. Dong, B. K. Xi, and P. Minnis, "A climatology of midlatitude continental clouds from the ARM SGP central facility. Part II: Cloud fraction and surface radiative forcing," J. Clim. **19**(9), 1765–1783 (2006).

Optics EXPRESS

86. M. D. Shupe, V. P. Walden, E. Eloranta, T. Uttal, J. R. Campbell, S. M. Starkweather, and M. Shiobara, "Clouds at Arctic Atmospheric Observatories. Part I: Occurrence and Macrophysical Properties," J. Appl. Meteorol. Climatol. **50**(3), 626–644 (2011).
87. P. Kollias, G. Tselioudis, and B. A. Albrecht, "Cloud climatology at the Southern Great Plains and the layer structure, drizzle, and atmospheric modes of continental stratus," J. Geophys. Res. Atmos. **112**(D9), D09116 (2007).
88. B. K. Xi, X. Q. Dong, P. Minnis, and M. M. Khaiyer, "A 10 year climatology of cloud fraction and vertical distribution derived from both surface and GOES observations over the DOE ARM SPG site," J. Geophys. Res. Atmos. **115**(D12), D12124 (2010).
89. C. M. Lo, J. M. Comstock, C. Flynn, "An atmospheric radiation measurements value-added product to retrieve optically thin cloud visible optical depths using micropulse lidar," DOE/SC-ARM/TR-077, U.S. Dep. of Energy, Washington, D. C.
90. X. Q. Dong, P. Minnis, and B. K. Xi, "A climatology of midlatitude continental clouds from the ARM SGP Central Facility: Part I: Low-level cloud macrophysical, microphysical, and radiative properties," J. Clim. **18**(9), 1391–1410 (2005).
91. J. Q. Zhang, X. A. Xia, and H. B. Chen, "A Comparison of Cloud Layers from Ground and Satellite Active Remote Sensing at the Southern Great Plains ARM Site," Adv. Atmos. Sci. **34**(3), 347–359 (2017).
92. R. Wood and C. S. Bretherton, "On the relationship between stratiform low cloud cover and lower-tropospheric stability," J. Clim. **19**(24), 6425–6432 (2006).
93. A. D. Kennedy, X. Q. Dong, and B. K. Xi, "Cloud fraction at the ARM SGP site Instrument and sampling considerations from 14 years of ARSCL," Theor. Appl. Climatol. **115**(1-2), 91–105 (2014).
94. G. G. Mace and S. Benson, "The vertical structure of cloud occurrence and radiative forcing at the SGP ARM site as revealed by 8 years of continuous data," J. Clim. **21**(11), 2591–2610 (2008).

1. Introduction

Cloud plays a significant role in the earth's climate system as it is inextricably connected to the atmosphere's radiative balance and hydrological cycle. Cloud greatly affects the Earth's radiation budget by not only reflecting the incoming solar shortwave radiation, but also trapping the outgoing terrestrial longwave radiation [1–12]. Cloud also regulates the atmospheric hydrological cycle and redistributes it by means of precipitation [13,14]. However, cloud feedback has long been identified as one of major uncertainties in understanding and predicting climate system due to its robust spatiotemporal variability and poor representativeness in climate models [15,16]. When considering the role of cloud in climate system, the exact information about cloud macrophysical properties such as cloud height, thickness and fraction is essential [17–25]. Therefore, better understanding cloud properties from observational view at various regions is essential [9,10,26-29].

Despite the decades of research efforts made to reduce the uncertainties in cloud properties over regional and global scales through active and passive sensors from ground-based, space-based and in situ observation platforms, the accurate assessment of cloud is still one of the biggest challenges in predicting any potential future climate change [30-32]. Passive sensors can provide only total column amounts of layer-relevant measurements [33, 34] and their retrieval accuracy suffers from various limitations [35], yet these disadvantages can be overcame by ground and space-based active remote sensors, such as lidar and radar [27,36,37]. The space-borne CALIOP can provide cloud and aerosol vertical distribution information on a global scale [38–42]. However, it is impossible to study the diurnal impact of particulate layer properties in the Earth system due to the limited temporal resolution [43]. Although lidar cannot penetrate some thick-low and -midlevel clouds because of severe attenuation, most mid- and high-level clouds can still be accurately observed e.g. [44]. Furthermore, lidar is more sensitive to optically thin targets when it is compared with the millimeter wave radar, e.g. [45]. Hence, ground-based lidar is a powerful equipment, which could meet the demands that are highly stable, accurate, precise and long-term continuous observations over a specified site, for investigating the main atmospheric constituents, such as cloud and aerosol [46].

With the development of lidar technologies, the relevant algorithms of atmospheric feature layer detection have also been continually proposed and improved. Aforetime, the cloud boundary was determined only relying on the difference between scattering from atmospheric particle layers and the background molecules [47] or slope of lidar signal [44,48]

Optics EXPRESS

using static thresholds. These methods need careful tuning to reject small backscatter enhancements caused by noise and aerosol returns, but for the technique described by Sassen and Cho [47], it avoids some of these problems and works more effectively in the upper troposphere. Winker and Vaughan [49] resolved cloud detection issue using the range-dependent thresholds only based on the attenuated scattering ratio, and the method can filter noise efficiently at high altitude level. As pointed out by Campbell et al. [50], the methods based on the highly dependent signal profiles may need abundant threshold modification when applied to intensive network data from different instruments. To avoid this issue, Campbell et al. [50] developed a threshold algorithm based on the statistical uncertainties of the signal profile, an independent variable, making it more easily transferable. And it can realize detection of cloud and aerosol simultaneously. However, the algorithm is attenuation limited for multilayer cloud scenes. Afterwards, Vaughan et al. [51] established an adaptive range-dependent threshold algorithm and applied the multi-resolution averaging scheme to detect cloud, aerosol and planetary boundary layers (PBL) for CALIOP, which can detect more cloud layers even for multilayer cloud situations. Based on different principle, continuous wavelet transform (CWT) analysis has been introduced to identify particulate layer structure in the lidar profile. This method could be not only used for boundary layer height analysis [52, 53], but also designed to retrieve the vertical distribution of cloud and aerosol [54]. Zhao et al. [55] firstly detected aerosol/hydrometeor layers based on semi-discretization processing (SDP) method and value distribution equalization (VDE) to minimize the impact of noise in lidar signal, then discriminated clouds and aerosols based on empirical threshold values. Liu et al. [56] combined the slope method and empirical threshold values to separate cloud from aerosol layer and used linear depolarization to identify cirrus cloud. However, there still have no universal particulate layer detection algorithm for lidar measurements without limitation. This is because there is no binary solution to analyzing signal returns for particulate layer structure across the laser emission spectrum [44, 50].

Recently, an automated feature detection and extinction retrieval (FEX) algorithm for Raman lidar (RL) at ARM sites was developed by Thorsen et al. [57] and Thorsen and Fu [58]. The approach of feature detection in FEX was to use multiple quantities (scattering ratios derived using elastic and nitrogen channel signals from narrow and wide fields of view, scattering ratio derived using only elastic channel, and the total volume depolarization ratio) to identify the atmosphere feature using range-dependent thresholds. The extinction retrieval of FEX, which is supported by a classification of feature types (aerosol, water cloud, ice cloud, rain and HOI), realized the best estimate of particulate backscatter and lidar ratios for all detected features. FEX is an iterative algorithm, where the extinction retrieval is not only required by both the feature classification and the multiple-scattering model, but also needed by feature detection and vice versa. FEX has good performance at detecting all major features due to using multiple quantities and classifying features reasonably owing to obtaining lidar ratio. However, for elastic lidars, dust aerosol was always mistakenly identified as ice cloud based on empirical thresholds relying on the atmospheric thermodynamic state and the feature's scattering properties (backscatter coefficient, and depolarization ratio). It is obvious that FEX is suitable for RL and high spectral-resolution lidar (HSRL) systems that can intrinsically separate signal returns from molecules and particulates, but not for the general elastic lidars.

The micropulse lidar (MPL) has been operated continuously for 8 years at SACOL since March of 2007. In addition, four intensive observation field campaigns have been carried out at sites of Minqin, Dunhuang, Zhangye and Jingtai, respectively. Thus, MPL has accumulated large and extremely valuable datasets for aerosol and cloud research during these periods. However, there have not been a uniform algorithm to retrieve the macrophysical, optical and microphysical properties of cloud and aerosol. Consequently, no standard cloud and aerosol products haven't been formed yet to explore more valuable information. MPL is only an elastic lidar, without Raman channel, which means the FEX algorithm cannot be used directly

Optics EXPRESS

to these data, but the variables available such as elastic scattering ratio and depolarization ratio could also be used for layer detection, and then layers also can be classified reasonably by combining the empirical thresholds determined by both the features' scattering properties and atmosphere's thermodynamics states with CWT method. In this study, an automated cloud and aerosol feature detection algorithm for MPL based on context-sensitive thresholds, which is modified from the FEX algorithm [57,58] and further uses the CWT analyses.

The SACOL MPL instrument and the modified layer detection and classification algorithm are described in section 2. Section 3 shows the two case studies, the evaluation of the CWT, and the description of samples and cloud macrophysical properties by applying the modified retrieval algorithm to MPL observations at SACOL. Summary and conclusions are given in section 4.

2. Instrument and methodology

2.1 SACOL site

The SACOL (35.946°N, 104.137°E, 1965.8 m) is located at the top of Tsuiying Mountain in Yuzhong campus of Lanzhou university, which is around 48 km from Lanzhou city. Figure 1 shows the topography of East Asia and the location of SACOL site. The SACOL site is located in a path of Asian dust long-range transportation [59,60]. Like the most observational sites over the northwest of China, the observation was obviously affected by frequent dust events in the spring. The Atmospheric observations at this permanent site began in 2006 with the objective to operate a combination of several instruments for measuring atmospheric radiation, wind, atmospheric temperature and humidity, clouds and aerosols as well as land-atmospheric interaction processes [61,62]. Following up these observations, the lidar system operated in 2007 and the advanced 8.6mm KAZR cloud radar collected data starting in 2013 [63].

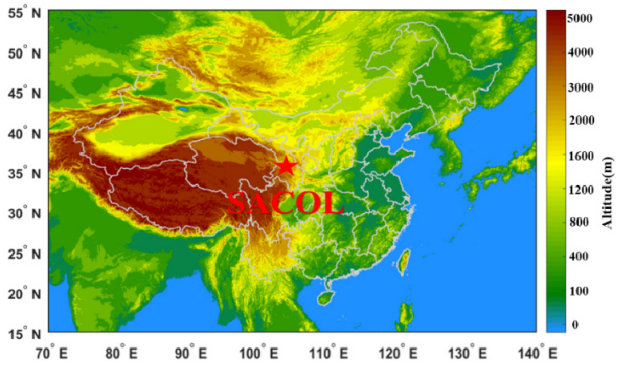

Fig. 1. Geographical coverage of East Asia (10–55° N, 70–140° E). The red pentagram shows the location of SACOL site in Northwest China.

2.2 MPL

The MPL-4B, manufactured by NASA Goddard Space Flight Center, is a safe, compact and maintenance-free lidar system for long-term measurements of vertical profiles of aerosol and cloud [64]. More detail information about the standard designs, site maintenance and calibration techniques of MPL and its characterization are given by Campbell et al. [65]. The data uncertainties related to the lidar instrument were depicted elaborately further by Welton and Campbell [66]. This lidar system at SACOL which have only one elastic backscatter channel of 527nm, has automatically and continuously operated since March of 2007. After September 2009, it is an upgrade of a pre-existing one, which could measures the polarization property of atmosphere particles. In addition, the vertical resolution was improved from 75m

Optics EXPRESS

to 30m, and temporal resolution still remained 1 minute. In this study, the observation data from March 2011 to February 2012 at SACOL were used.

2.3 ERA-Interim data

To calculate expected molecular signal and distinguish the cloud phase and aerosol, the variables like temperature, pressure and humility profiles were also needed. Here, these variables were obtained from ERA Interim reanalysis produced by the European Centre for Medium-Range Weather Forecasts (ECMWF), covering the data-rich period since 1979 and continuing to be updated in real time (http://apps.ecmwf.int/datasets/). Its spatial resolution is 0.125° and temporal resolution is 6 h. It has 37 vertical levels from 1000hPa to 1hPa [67]. To verify the reanalysis data, the comparison of temperature and humility profiles between radiosonde at Yuzhong station (52983, 35.87°N, 104.15°E, approximately 8.54 km away from SACOL site), which is launched at 08:00 and 20:00 each day, and the nearest pixel (36.00°N, 104.125°E, about 6.11km away from SACOL site) of ERA-Interim reanalysis were performed at the same moments. The results suggest that ERA-interim could provide reliable vertical profiles of temperature and humility. Hence, it was adopted to represent the atmosphere conditions at SACOL in this work.

2.4 Data analysis and methodology

The fundamental of feature layer detection in this work is based on the signal detection theory in this work [e.g., 57,68]. Simply, atmosphere particle layers can be detected by setting a threshold in the presence of two probability distributions that describe the expected molecular signal and measured lidar signal, respectively. Figure 2 displays the flowchart of modified layer detection and classification algorithm that is iterative. The automated cloud and aerosol feature detection algorithm is developed for the MPL based on context-sensitive thresholds, which is modified from the FEX algorithm [57,58], and further uses the CWT analyses. Here we emphasize on the processes of the methodology: calculating ratios and identifying feature layers (section 2.4.1), and distinguishing and revising layer types (section 2.4.2).

2.4.1 Calculating ratios and identifying feature layers

In this study, two variables available including the elastic scattering ratio and linear depolarization ratio were used to identify atmospheric particulate layers.

The lidar equation owing to elastic backscattering [69] can be written as:

$$\mathrm{P}(\mathrm{r}) = \mathrm{C}\frac{E}{r^2}O(r)\left[\beta_m(r)+\beta_p(r)\right]e^{-2\int_0^r \alpha_m(r')dr'}\,e^{-2\int_0^r \alpha_p(r')dr'} \tag{1}$$

where C is system calibration constant, E represents the emit energy of the laser pulse, $O(\mathrm{r})$ is the overlap function that exhibits the conflicts between the outgoing laser beam and the receiver field-of-view (FOV). $\beta_m(r)$ and $\beta_p(r)$ are the molecular and particulate backscatter coefficients, respectively. The two exponential expressions in the equation are the transmittance due to molecules and particulates, where $\alpha_m(r)$ and $\alpha_p(r)$ are the molecular and particulate extinction coefficients, respectively; P(r) is the total lidar signal with correction of deadtime, afterpulsing, background noise [65], which is the main input of this algorithm. For MPL with polarization, P(r) was also written as [70]:

$$\mathrm{P(r)} = 2\mathrm{P_{cr}(r)} + \mathrm{P_{co}(r)} \tag{2}$$

where $\mathrm{P}_{cr}(\mathrm{r})$ and $\mathrm{P}_{co}(\mathrm{r})$ represent the signals in “cross-polar” and “co-polar” channels, respectively.

Optics EXPRESS

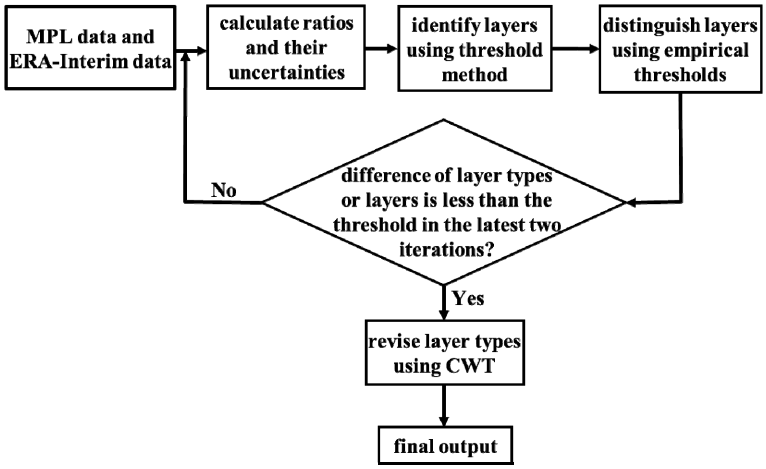

Fig. 2. Diagram showing the processes in the modified layer detection and classification algorithm for MPL.

The molecule backscatter $\beta_m(r)$ can be accurately modeled and expressed as [71]:

$$\beta_m(r) = N(r)\frac{d\sigma_{Ra}}{d\Omega_\pi} \tag{3}$$

where $N(r)$ is the molecular number concentration profile. $d\sigma_{Ra}/d\Omega_\pi$ is the differential backscatter cross sections for Rayleigh scattering.

The scattering ratio is defined as the ratio of the total (particulate and molecular) backscatter to the expected pure molecule backscatter. It can be acquired by combining the Eq. (1)-(3).

$$SR_E(\mathrm{r}) = C_E \frac{2\mathrm{P}_{cr}(\mathrm{r}) + \mathrm{P}_{co}(\mathrm{r})}{\frac{E}{r^2}O(r)N(z)e^{-2\int_0^r \alpha_m(r')dr'}e^{-2\int_0^r \alpha_p(r')dr'}} \tag{4}$$

$$C_E = 1/\left(C\frac{d\sigma_{Ra}}{d\Omega_\pi}\right) \tag{5}$$

Correspondingly, the expected clear-sky scattering ratio can be expressed as:

$$\mathrm{SR}_E^m(r) = \mathrm{A}(r)\left(2\mathrm{P}_{cr}^m(\mathrm{r}) + \mathrm{P}_{co}^m(\mathrm{r})\right) \tag{6}$$

where $\mathrm{A(r)}$ contains all other terms in scattering ratio that have ignorable random noise when compared with the signal noise; the superscript "m" of different quantities denotes the relevant different expected molecular values.

For MPL, to calculate the linear depolarization ratio, the so-called MPL depolarization ratio need be calculated [70] firstly:

$$\delta_{MPL}(r) = \frac{\mathrm{P}_{cr}(\mathrm{r})/O_{cr}(\mathrm{r})}{\mathrm{P}_{co}(\mathrm{r})/O_{co}(\mathrm{r})} = \frac{\mathrm{P}_{cr\_o}(\mathrm{r})}{\mathrm{P}_{co\_o}(\mathrm{r})} \tag{7}$$

Optics EXPRESS

where $\mathrm{P}_{cr\_o}(\mathrm{r})$ and $\mathrm{P}_{co\_o}(\mathrm{r})$ are the lidar signals corrected by overlap functions of $O_{cr}(\mathrm{r})$ and $O_{co}(\mathrm{r})$ in the "cross-polar" and "co-polar" channels, respectively; Then the linear depolarization ratio can be acquired:

$$\delta(\mathrm{r}) = \frac{\delta_{MPL}(r)}{\delta_{MPL}(\mathrm{r})+1} = \frac{\mathrm{P}_{cr\_o}(\mathrm{r})}{\mathrm{P}_{co\_o}(\mathrm{r})+\mathrm{P}_{cr\_o}(\mathrm{r})} \tag{8}$$

Similarly, the expected clear-sky linear depolarization ratio can be written as:

$$\delta^{m}(r) = \frac{\mathrm{P}^{m}_{cr\_o}(\mathrm{r})}{\mathrm{P}^{m}_{co\_o}(\mathrm{r})+\mathrm{P}^{m}_{cr\_o}(\mathrm{r})} \tag{9}$$

To identifying aerosol and cloud layers, both the expected clear-sky ratio and corresponding noise are needed, thus, the molecular signal and random noise in each channel are demanded.

The signal-to-noise (SNR) is a parameter to assess lidar performance. It is generally defined as:

$$\mathrm{SNR}(\mathrm{r}) = \frac{\mathrm{P}(r)}{\sigma(r)} \tag{10}$$

For MPL, SNR can also be showed as [72]:

$$\mathrm{SNR}(\mathrm{r}) = \frac{N\mathrm{P}(r)}{\sqrt{N\mathrm{P}(r)}+\mathrm{P}_{bkg}N} \tag{11}$$

where N is the number of accumulated shots in a temporal shot average and P_{bkg} is the received power due to the solar background.

Naturally the signal noise in each channel can be calculated as:

$$\sigma(\mathrm{r}) = \frac{\mathrm{P}(r)}{SNR(r)} = \sqrt{\frac{\mathrm{P}(r)}{N}}+\mathrm{P}_{bkg} \tag{12}$$

Here, $\mathrm{P}(r)$ indicates the measured lidar signal. If it is replaced by the molecular lidar signal, the random noise of expected clear-sky signal can be required by Eq. (12)

$$\sigma^{m}(\mathrm{r}) = \sqrt{\frac{\mathrm{P}^{m}(r)}{N}}+\mathrm{P}_{bkg} \tag{13}$$

By propagation of uncertainty [73], the noises of two ratios in the Eq. (6) and (9) are:

$$\sigma_{\mathrm{SR}^{m}_{E}}(r) = \mathrm{A}(r)\sqrt{4\sigma^{2}_{\mathrm{P}^{m}_{cr}}(r)+\sigma^{2}_{\mathrm{P}^{m}_{co}}(r)} \tag{14}$$

$$\sigma_{\delta^{m}}(r) = \delta^{m}(r)\sqrt{\frac{\sigma^{2}_{\mathrm{P}^{m}_{cr\_o}}(r)+\sigma^{2}_{\mathrm{P}^{m}_{co\_o}}(r)}{\left[\mathrm{P}^{m}_{co\_o}(\mathrm{r})+\mathrm{P}^{m}_{cr\_o}(\mathrm{r})\right]^{2}}+\frac{\sigma^{2}_{\mathrm{P}^{m}_{cr\_o}}(r)}{\left[\mathrm{P}^{m}_{cr\_o}(\mathrm{r})\right]^{2}}} \tag{15}$$

The range-dependent threshold profile for two ratios can be obtained:

$$\tau(\mathrm{r}) = R^{m}(r)+C*\sigma_{R^{m}}(r) \tag{16}$$

where $R^{m}(r)$ is ratio, $\sigma_{R^{m}}(r)$ is uncertainty of ratio, C is constant coefficient and $\tau(\mathrm{r})$ is the context sensitive threshold set to identify cloud and aerosol layers. Portions of the

Optics EXPRESS

measured ratio profiles that exceed the threshold profile $\tau(r)$ are considered to potentially contain atmospheric particle layers. Additionally, spatial filter is still used to reduce false detections, that is, the pixels where the overlap probability P between the expected molecular signal and measured signal distributions (Ref [57], Fig. 1.) is more than the threshold determined empirically are thought as false detection and changed as clear sky. Based on the fact that the wavelength of MPL laser operates is in a region of maximum solar energy, so it is obvious that MPL observation must contend with a large amount of additional noise during daytime [74]. Here, the different thresholds for C in the depolarization ratio and for P in the scattering ratio were used during day and night [20] to detection complete particle layers. Of course, the additional modification was needed to revise the detected particle layers. It was noticeable that scattering ratio can produce pseudo big values due to extinction iteration, which can identity some fake particle layers in the processing of methodology. So the scattering ratio in the first iteration was used in each circulation to identity reasonable particle layers, if the particle layers detected in the second iteration increases by 1% of that in the first iteration empirically. In the meanwhile, the big value area (>10) of scattering ratio in the last iteration is used to avoid missed particle layers. For the particle layers detected by depolarization ratio, once the Nth pixel with the depolarization ratio greater than 0.5 in each profile from bottom to top, the pixels between Nth to top were removed.

2.4.2 Distinguishing and revising layer types

In this work, particle layer types are essential for extinction retrieval and modeling multiple scattering. Thus, classifiers are used to differentiate detected particle layers as aerosol, liquid cloud, or ice cloud.

Previous studies realized particle layer classification by combining different remote sensors [44,75]. For lidar, the classification methods are neural networks, probabilistic methods and empirical thresholds [76]. The neural networks and probabilistic methods are more sophisticated. Here, considering that MPL contains only one elastic channel, particle layer classification could not simply rely on a set of rules and empirical thresholds in the FEX algorithm for the Raman lidar [57,58], but a further analyses using the CWT method could help distinguish cloud from aerosol, especially for dust events.

In this work, the empirical thresholds were determined based on optical properties such as backscatter coefficient, linear depolarization ratio mainly, as well as atmospheric thermodynamic state such as temperature, wet temperature. Here the solution of Fernald [77] was used to retrieve profiles of the particular extinction and backscatter. And the assumed lidar ration values for aersol, water cloud and ice cloud are 50sr, 18sr, and 22sr [58,78,79]. Comparing with the threshold (0.09) at ARM sites [58], the higher threshold of depolarization ratio (0.21) used in this work may result from more nonspherical particles at SACOL in northwest of China. As mentioned above, SACOL is in the path of long-range dust transportation, where the dust happens frequently in early spring and late winter. The dust aerosol with bigger depolarization ratio can be mistakenly identified as ice cloud if only relying on the empirical thresholds without best estimation of lidar ratio. To distinguish dust aerosol from ice cloud, the boundary of ice cloud layer must be found, which can be achieved by continuous wavelet transform (CWT). This method is based on the high correlation between the lidar signal and the “Mexican hat” wavelet shape [54]. The CWT was applied to the scattering ratio due to the relatively striking contrast between aerosol and cloud in it. In this work, the mean CWT coefficients along the lines were used to avoid the bias caused by the selected coefficient particularly. The threshold of CWT coefficients was selected as 11 to discriminate cloud layer from the aerosol layer. Under this condition, the peak of cloud layer could be found accurately, while the top and base location need to be modified. The revised top was defined as the peak height adding the number of bins with the values of scattering ratio greater than 6 in the range of peak and top for each profile. The revised base height was defined as the peak height subtracting the number of bins with the values of scattering ratio

Optics EXPRESS

greater than 8 in the range of peak and base for each profile. Ultimately, the particle layers was classified reasonably.

3. Results and discussion

In this paper, the four seasons are defined as spring from March to May (MAM), summer from June to August (JJA), autumn from September to November (SON) and winter from December to February (DJF). The following shows the two cases by applying the modified feature detection algorithm (3.1), the evaluation of the use of CWT (3.2), the description of observational samplings (3.3), and the corresponding statistical results of cloud macrophysical properties (3.4).

3.1 Case studies

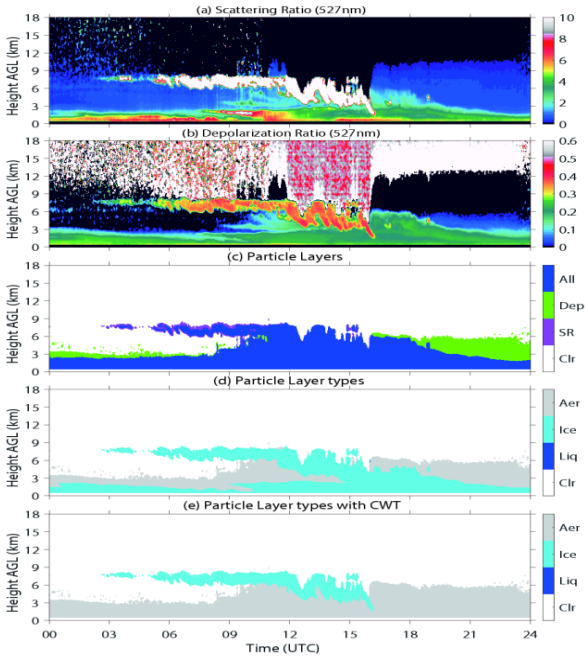

Fig. 3. (a) Scattering ratio, (b) linear depolarization ratio, (c) particle layers where each color represents a different combination of the two ratios: scattering ratio (SR, purple), depolarization ratio (Dep, green) and both ratios (All, blue), (d) particle layer types which show liquid cloud (blue), ice cloud (black) and aerosol (gray), (e) particle layer types with CWT, the colors indicate the same meaning as (d). The date is for March 7, 2011 at SACOL.

Figure 3 shows a case result of the algorithm in dust incident on March 7, 2011. In Fig. 3(a) and Fig. 3(b), both scattering ratio and depolarization ratio are high around 3-8km during 03:00-16:00 UTC, which demonstrates this is ice cloud. The value of depolarization ratio around 0-2km is about 0.21-0.25 and routine synoptic record from visual observation by station personnel on that day was written as floating dust. Thus, it is obviously that it is a dust incident. On this day, the aerosol layer exists throughout the whole day. The dust aerosol in 00:00-09:00 UTC is relatively weak, which originates from the gradually weaken dust in March 6. After 09:00 UTC, the height of dust aerosol layer became higher, which buried the low part of ice cloud until the ice cloud passed by SACOL about 16:00 UTC. Then, the strong dust lasted for two hours and gradually weakened at 18:00 UTC. In Fig. 3(c), the combination of scattering ratio and depolarization ratio can capture the particle layers sufficiently. With the advantages of respective detection, both can detect cloud reasonably, but depolarization ratio is more adept in detecting aerosol in this work. Figure 3(d) visualizes the particle layer types relying on empirical thresholds based on depolarization ratio and backscatter

Optics EXPRESS

coefficient. It is obvious that dust aerosol was mistaken as ice cloud. The similar mistaken scenes are frequent over the dust source regions and near dust source regions [80–82]. To avoid the problem, CWT that can detect discontinuities (base, top and peak) of individual particle layer based on scattering ratio in the last iteration was used to find cloud boundary in the dust aerosol, which is showed in Fig. 3(e). By comparing Fig. 3(a), (b) with cyan area in Fig. 3(e), it is obvious that ice cloud and dust aerosol can be differentiated well by combining empirical thresholds with CWT. It exhibits robust detection capacity in classifying layer types in the whole data, especially for distinguishing ice cloud from dust aerosol in dust events during spring and late winter.

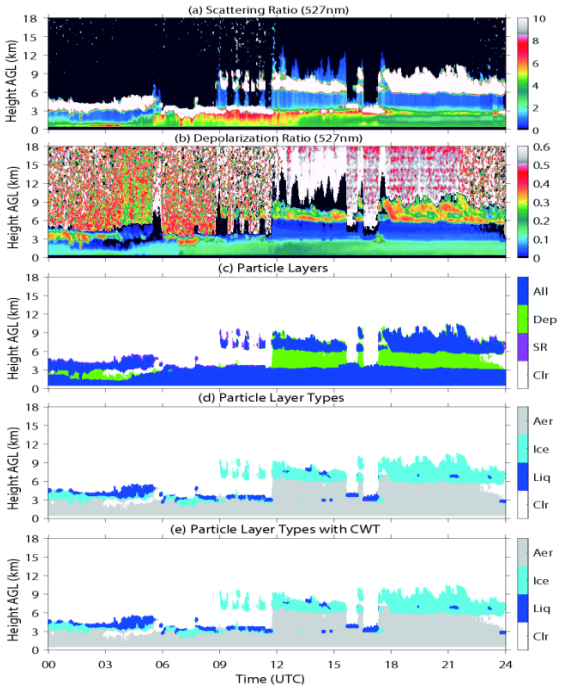

Fig. 4. The same as Fig. 3., but for June 04, 2011 at SACOL.

Figure 4 shows the retrieval result of a non-dust situation for MPL on June 04, 2011. By observing Fig. 4(a) and Fig. 4(b), there exist low and high clouds on this day. The low mixed phase cloud around 3-5 km during 00-12:00 UTC originates from the high ice cloud that passed through SACOL at 15:00 UTC on June 03, 2011. The high mixed phase cloud, mainly ice crystal, is around 6-9 km during 09-24:00 UTC. And the low and high clouds passed through SACOL overhead simultaneously during 09-12:00 UTC. Aerosol layer exists throughout the day, which is topped by clouds. The aerosol is weak during 00-06:00 UTC, strengthens and interacts with low cloud during 06-18:00 UTC, and is weaker and delaminates into two layers during 18-24:00 UTC. In Fig. 4(c), all major layers are detected, including some small isolated parts about 8 km during 09-12:00 UTC. It is obvious that the combination of both ratios can capture the particle layers very well. Figure 4(d) pictures particle layer types only relying on empirical thresholds. The depolarization ratio values of supercooled water in mixed phase cloud during 04-05:00 UTC are less than 0.1 and ice cloud during 18-19:00 UTC are more than 0.25, while the scattering ratio values of the clouds are more than 10. This demonstrates that the algorithm can realize the reasonable classification in the detected atmospheric particle layers.

As described above, CWT can avoid the problem that dust is mistaken as ice cloud in classifying layer types only relying on empirical thresholds with elastic lidar. And the result of layer types with the combination of CWT and empirical threshold method is consistent

Optics EXPRESS

with the result of layer types without CWT (only relying on the empirical threshold method) in non-dust events. In this case, the difference of cloud pixels between Fig. 4(d) and Fig. 4(e) relative to the cloud pixels in Fig. 4(d) is only 2.14% and the difference of cloud base/top height is only −0.59%/-0.14%. They are all thought as reasonable bias.

3.2 Evaluation of the performance empirical threshold method along with CWT

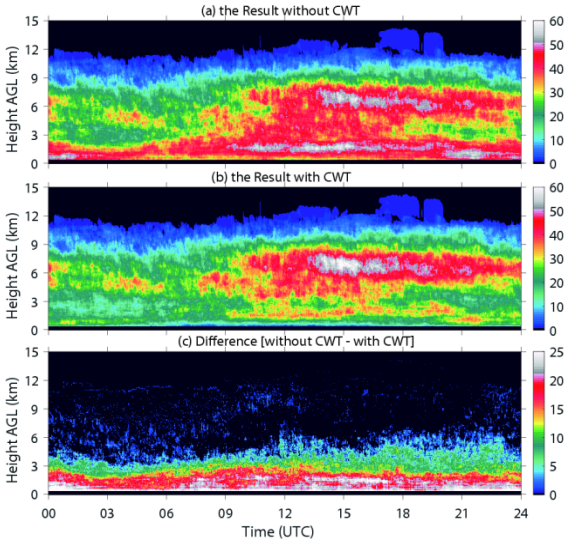

Fig. 5. Diurnal variation in accumulated cloud pixels (absolute amount) observed by the MPL for (a) the result without CWT,(b) the result with CWT and (c) the difference between the both results at SCOL from March 2011 to February 2012.

The accumulated cloud pixels for the results without/with CWT and the difference between them during 2011 are shown in Fig. 5. Both Figs. 5(a) and 5(b) show that more clouds occur during night than during day. Zhao et al. [55] also reported the same diurnal variation for cloud. Considering the characteristics of MPL, the difference is at least partly due to the effects of solar background noise on lidar signal during daytime [83]. By comparing Fig. 5(a) with 5(b), the result without CWT visualizes the more so-called low clouds within 3 km, which is shown in Fig. 5(c). This result demonstrates that the obvious difference exists between the results without and with CWT part in our modified method. As shown by Fig. 3, this difference is very likely caused by dust aerosol in low latitudes.

Optics EXPRESS

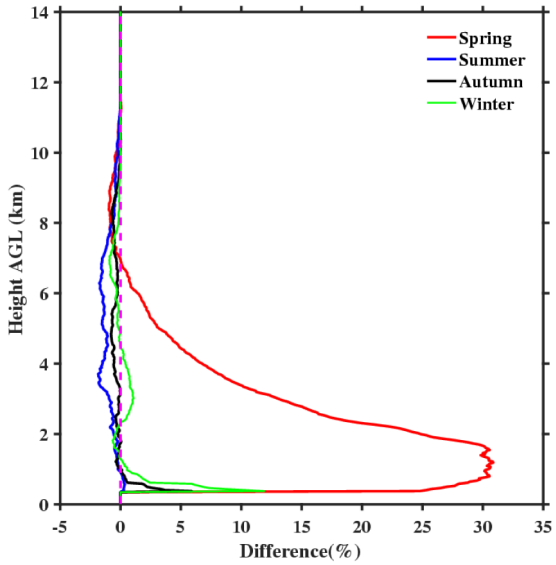

Fig. 6. The seasonal vertical distribution of difference between the results without/with CWT relative to the profiles available (solid lines, relative amount) and while the reference "0" line (the dashed line).

To further verify what causes the difference shown in Fig. 5(c) in detail, the seasonal vertical distribution of difference percentage that is the absolute difference relative to the number of profiles available was illustrated in Fig. 6. As mentioned above, the dust events are always measured during late winter and spring at SACOL site, so Fig. 6 is in accord with our expectations: the largest difference (about ~30% within 1 to 2 km) below 8 km can be found in spring, which is caused by dust aerosol mistaken as ice cloud without CWT. The obvious difference (about 7% within 0.36 to 0.6 km) below 1 km also occurs in winter, which suggests that the dust aerosol may be weaker in winter than in spring in 2011 at SACOL. Due to the fixed scaling coefficient selected for different center heights in CWT, so it may sometimes omit few cloud pixels (mainly water cloud, about 3% within 0.36 to 0.54 km) with range of 0.36 to 0.6km in autumn. The bias, however, is negligible for the whole data. In summer, CWT detected more cloud pixels (about −1% within 3 to 7.5km) within the range of 2 to 8 km, which exhibits that CWT can supplement cloud detection omitted by the empirical threshold method. That is shown in higher accumulated cloud pixels around 6-8 km from 14:00 to18:00 UTC in Fig. 5(b), when compared with Fig. 5(a).

3.3 Description of samples

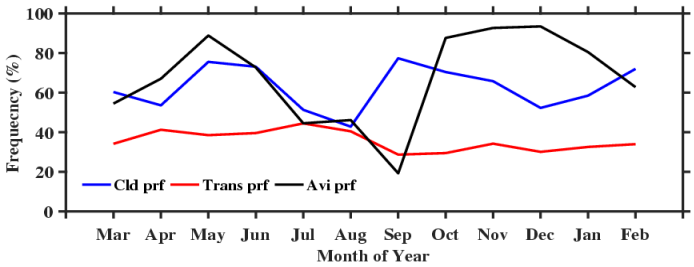

Fig. 7. "Avi prf" (black line) presents the total number of profiles available relative to expected total number of profiles in each month; "Cld prf" (blue line) presents the total number of cloud profiles relative to the total number of profiles available, namely cloud fraction (CF); "Tans prf" (red line) presents the number of fully transparent profiles relative to the total number of cloud profiles.

Optics EXPRESS

Figure 7 shows that the monthly variation of "Profiles Available", "Cloud Profiles" and "Transparent Profiles" during one year. For the profiles available, the MPL data suffered from occasional quality issues during our analysis period, which are identified and removed. As a result, the total number of profiles available is 224129 in 2011. Differences in sampling during analytical time period can cause observations to favor the cloud properties of a particular month/season. In the view of monthly variation, it is noted that profiles available are little during July-September in the whole year, especially for September (19%, only six day observation data). The analysis of cloud base height (CBH) and CF was based on the profiles available.

CF is defined as the percentage of cloud profiles within a specified sampling period (e.g., a month or a season) regardless of the number of cloud layers. Although ground-based-lidar-derived CFs represent only a pencil beam of the sky that depends on the advection of clouds overhead, they have been found to be statistically representative in long-term averages (i.e., monthly) of the entire sky when compared with long-term satellite and surface observations [84,85]. CF exhibits strong seasonal variability with the maximum value observed in autumn (68%), the minimum in winter (58%) and a secondary minimum in summer (59%). In the view of meteorological variations, the relatively high surface pressure, cold temperatures, and low moisture in the winter, especially for December, can induce the low CF during the winter [86].

But for summer, broken boundary layer clouds may be responsible for the low CF [87]. The high frequent occurrence of low-level clouds (as shown in Fig. 9) results in the highest CF during autumn months in the year. However, the results of previous studies [55,84,88] in mid-latitude sites indicate that the maximum/minimum CF value is in winter/summer. This may mainly results from different meteorological conditions for different sites, but may also partly result from the sampling differences.

For the transparent profiles, they only contain the profiles that lidar signal was not completely attenuated by cloud layers. Several procedures are carried out based on scattering ratio profiles to identify these profiles [89]. First, the cloud free interval is not determined above cloud until the scattering ratio in the lowest bin above cloud range is within 10% of a numerical fit to the scattering ratio in the next 8 range bins. Otherwise the lowest bin is discarded and an additional bin is added at the top. It is noted that the requirement that scattering ratio of the lowest bin is not more than 10 and the decrement rate of scattering ratio among the lowest four bins is within 10% needs to meet. Second, if at least 4 points (120 m) above the cloud layer coincide to the demand that the decrement rate of scattering ratio is within 10%. It is then determined that the MPL signal was transparent. The statistics of cloud geometrical thickness (CGT) and cloud layers per profile are only derived from the data set of transparent profiles. In the view of seasonal variation, the minimum (31%) of the percent of transparent profiles are in autumn when the CF is maximum. This may suggest that the large-scale horizontally stratiform clouds are usually opaque for lidar signal in autumn.

3.4 Statistical results

Considering severe attenuation in lidar signals by thick clouds, the analysis of CBH detected in this study refers to the analysis of the first cloud layer base detected from the ground regardless of the number of cloud layers detected.

In Fig. 8, the little difference between mean and median values of monthly CBH suggests that monthly distribution of CBH may be normal although the same general trends are apparent [56,85]. The spread of CBH is largest in May and least in January for all day. By comparing the CBH in the day and night, the spread of CBH is more striking in day during May, while there is almost no difference in spread between day and night in January. The monthly mean CBH values are more than the yearly average during April-August period and less than the yearly average during September-March period. This results in strong seasonal CBH variability with a maximum value of 4.66 ± 1.95km in summer and a minimum value of

Optics EXPRESS

3.34 ± 1.84km in autumn. However, the result shows that the different seasonal patterns in CBH, i.e., maximum/minimum values in summer/winter, at other mid-latitude sites [56,90]. In autumn, there is higher frequent stratus cloud between 0 and 2 km (shown as in Fig. 9(c) and Fig. 9(d)), which can induce CBH to be lower directly, in autumn than during winter (3.46 ± 1.60km). The annual average CBH values are 3.87 ± 2.18km (4.05 ± 2.19) for day (night). The highest annual mean CBH was found during the night.

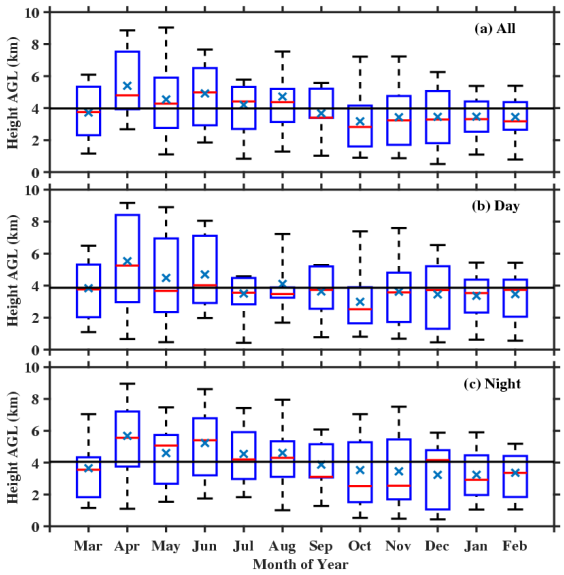

Fig. 8. Monthly mean CBH for (a) all day, (b) day, and (c) night from March 2011 to February 2012 at SACOL. Box and whisker plots include the median (red line in the box), 25th and 75th percentiles (bottom and top of the box), 5th and 95th percentiles (bottom and top of the whisker), the mean (multiplication sign) and annual means (black lines).

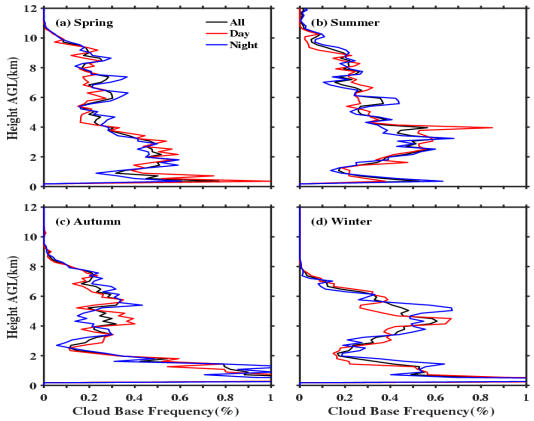

Fig. 9. Vertical variation in the frequency of CBH occurrence during (a) spring, (b) summer, (c) autumn, (d) winter from March 2011 to February 2012 at SACOL site. Black lines are for the cloud during the all day, red lines are for day and blue lines are for night. CBHs were averaged over 0.18 km in the vertical direction.

Figure 9 shows vertical frequency distributions of CBH seasonally during the year. By comparing the seasonal variation in day with in night, it is obvious that the whole variation trends are very consistent even though there exists some differences in certain heights. It suggests that day and night have little influence on the vertical distribution of CBH. In the view of seasonal variation, there is a triple-mode pattern in spring and summer. The first

Optics EXPRESS

narrow peak is boundary layer clouds (≤ 1km), the second obvious peaks lie around 2 km and 3.5 km and the third group of peaks are around 5.5-11km and 7-11 km in spring and summer, respectively. This implies that the dominant cloud types may be convective clouds and cirrus in summer and spring. In autumn and winter, the distribution of CBH shows the obvious bimodal and the higher peak shows difference with narrower height range and wider numerical scope in winter. This suggests that the prevalent cloud types are stratus and altocumulus cloud in autumn and stratiform clouds including status and altostratus in winter [32,44,]. The similar vertical CHB distribution is also observed by Zhao et al. [55], Lewis et al. [43] and Zhang et al. [91]. In the mid-latitude, the larger low-level cloud fraction is associated with greater estimated inversion strength (EIS) [92]. It is suggested that EIS is least in summer and greatest in autumn in the low troposphere in 2011 at SACOL.

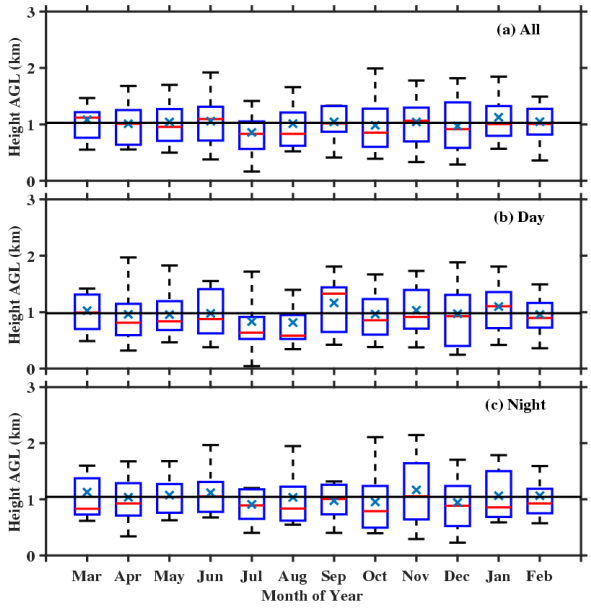

Fig. 10. The same as Fig. 8, bur for CGT for transparent profiles only.

Figure 10 visualizes CGT monthly variation during the all day (A), day (D) and night (N) for transparent profiles only. CGT is simply the difference between cloud top and cloud base height based on the transparent profiles. The spread of CGT is largest in October and least in March and September for all day. By comparing the CGT in the day and night, the spread of CGT is more striking in night during October and smaller in night in September, while there is almost no difference in spread between day and night in March. The monthly mean values of CGT for all day are below the yearly average in July, August, October and December. This may result from the high frequency isolated thin cirrus in June and July and prevalent stratus cloud in October and December. The cloud is generally slightly thicker during winter (1.05 ± 0.43km) than during summer (0.99 ± 0.44km). This suggests that cloud layers are thicker than warm ones. The mean annual cloud thickness is 1.03 ± 0.41km (A), 0.98 ± 0.45km (D) and 1.05 ± 0.48km (N). The cloud is thicker during night than during day. These are consistent with the result at SGP site [90].

Optics EXPRESS

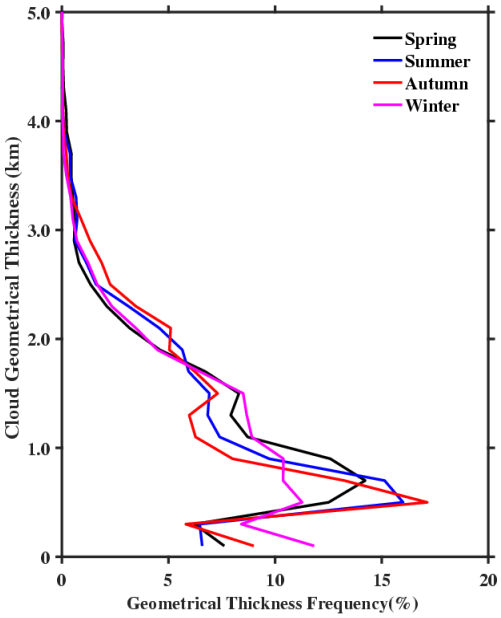

Fig. 11. The frequency distribution of CGT at 0.2 km intervals in seasonal variation during (a) spring (black line), (b) summer (blue line), (c) autumn (red line), (d) winter (purple line) from March 2011 to February 2012 at SACOL site for transparent profiles only.

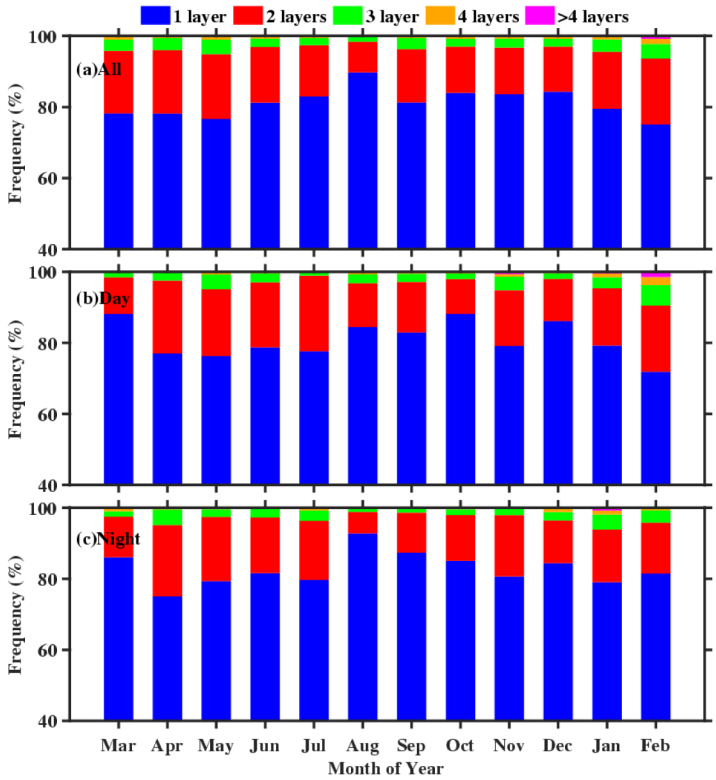

Fig. 12. Monthly variation in frequency of number of cloud layers in the transparent profiles such as single-layer (blue), two layers (red), three layers (green), four layers (orange) and more than four layers (magenta) for the all day (A), day (D) and night (N) at SACOL.

Optics EXPRESS

The seasonal frequency distribution of CGT between 0 and 5 km is illustrated in Fig. 11 based on the transparent profiles only. The distribution of CGT performs bimodal style, with low peak at 0.5 km and high peak at 1.5 km in four seasons. Especially for winter, the low peak value is distinctly less than other peak values of the other three seasons, and has little difference with the high peak values of winter. Due to the limited detectivity of lidar, the detected CGT is rarely more than 3 km in the transparent profiles. It is noticeable that there are big frequency values at 0.1 km in four seasons, which may be caused by the broken clouds detected in algorithm such as the clouds in the case 2 around 9 km during 9:00-10:00 UTC on June 04, 2011. Of course, noise can be occasionally mistaken as broken clouds and a piece of very weak cloud can be classified as several broken clouds in the algorithm.

Figure 12 shows the monthly variation in frequency of number of layers in the transparent profiles for the all day (A), day (D) and night (N). The single-layered clouds (81%) is dominated in the MPL-detected clouds, especially for nighttime. This is consistent with the result (80%) of Zhao et al. [55] at SGP site for MPL. In the view of monthly variation, more than 75% of clouds are single-layered system in each month; the two-layered clouds are more than 10% in each month except for August; the three-layered clouds are about 2%-4% in each month; the multi-layer (>3 layers) clouds happens more frequently during winter than the other seasons. The latter may be related to more broken clouds in winter shown in Fig. 11.

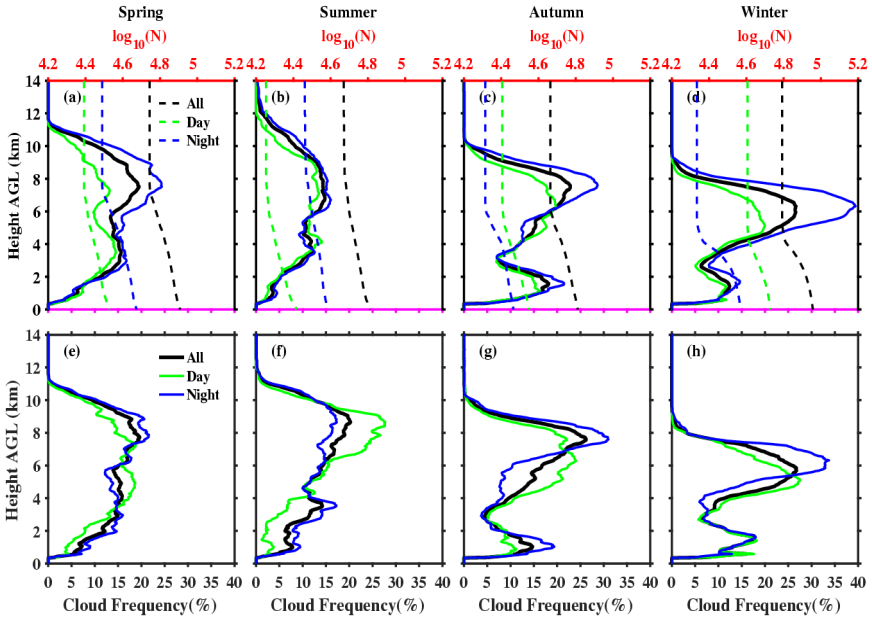

Fig. 13. Vertical variation of the CF (solid lines, down axis of (a)-(d)) and accumulated transparent (cloud + clear-sky) pixels N (dashed lines, top axis of (a)-(d)) in the transparent area and the CF in transparent profiles ((e)-(h)).

The seasonal vertical distributions of the CF and accumulated transparent pixels in the transparent area (Fig. 13(a)-(d)) and the CF in the transparent profiles (Fig. 13(e)-(h)) for all day (A), day (D) and night (N) were shown. The transparent area is defined as the combination of pixels if the lidar signal is not completely attenuated in profiles. The accumulated transparent pixels decreases with height based on the ground-based MPL observation. Overall, there is obvious bimodal distribution with a low peak located near the boundary layer and a high peak located in the upper troposphere in both CF definition profiles. The similar bimodal vertical distribution was documented by Mace et al. [94], Xi et al. [88], Kennedy et al. [93] and Zhang et al. [91] at SGP site. It's obvious that the upper-troposphere cloud layers dominate the heating of the troposphere, while lower-level clouds

Optics EXPRESS

provide a largely counterbalancing cooling influence. Thus, the combination of these two cloud types may result in little net atmospheric cloud radiative effect [94].

In the view of seasonal variation, the two peaks in the both CF definition profiles show differences in different seasons. The low peak is around 3-4 km and high peak is around 7-9 km in spring and summer, while the low peak is around 1-2 km in autumn and winter and the high peak is around 8 km in autumn and 6 km in winter. In Fig. 13(a)-(d), the distribution of cloud layer in the summer can extend to higher altitude (at ~13 km) than those in other seasons, which is due to a deeper troposphere and the more frequent convective storms [82]. Small frequency values located below 2 km occur in summer when comparing with the other seasons because stratus clouds are seldom seen then [90]. For the CF in the transparent profiles, the higher peak has a greater cloud frequency value, which implies that lidar signal can mainly passes through the high clouds such as cirrus, especially in summer and autumn.

In the Fig. 13(a)-(d), there is little diurnal difference of low-level clouds seasonally, while the most and least diurnal difference of high-level clouds occur in winter and spring, respectively. On the whole, the more clouds are observed in night than in day except that the more clouds happens within 4-6 km in day than in night during summer and autumn. This may result from the lidar detection characteristic, that is, lidar signal was effected severely by solar background noise during day on the condition that the opaque clouds are alike in day and night. Thorsen et al. [83] reported that the ground-based RL observes more ice cloud in night that in day at Atmospheric Radiation Measurement (ARM) Darwin site (12.325°S, 130.891°E). Zhao et al. [55] portrayed that more high-level clouds occur in night than in the day at Taihu site. These results confirm that more clouds may actually occur at night. That more clouds occur for night than day, especially at high altitudes, means that they would trap more longwave radiation within the atmosphere during nighttime and cause weak diurnal variations in temperature. In the Fig. 13(e)-(h), the least and most diurnal difference of low-level clouds happen in winter and summer, respectively, while the most diurnal difference of mid-level clouds and high-level clouds occur in autumn and winter, respectively. The more clouds are observed in night than in day during spring, autumn and winter except that the more clouds occur in day than in night within 3-7km. Especially for summer, the more clouds happens in day than in night within 5-10km and it is contrary at other altitudes.

Although the different defined CFs reflect different diurnal and seasonal variation in vertical distribution of CF in some altitudes, they are still very important for the local radiative budget at the SACOL site and should be considered when studying cloud radiative forcing.

4. Summary and conclusions

An automated cloud and aerosol layer detection algorithm has been developed for MPL, which is modified from the FEX algorithm with further use of the CWT. It realizes the particle layer detection using scattering ratio and depolarization ratio relying on the range-dependent thresholds, and makes particle layer classification by combining the 2-D empirical thresholds guided by depolarization ratio and backscatter coefficient and CWT. The CWT makes up the drawback of empirical thresholds with elastic lidar in classifying particle layers. The modified algorithm was applied to one year of MPL data at China SACOL site and the detection results and corresponding analyses confirmed the robust performance of the modified algorithm for MPL.

The temporal variation and vertical distribution of cloud macrophysical properties such as CBH, CGT and CF have been examined based on the results of the modified algorithm. At SACOL site, the maximum/minimum CBHs were found in summer (4.66 ± 1.95km)/autumn (3.34 ± 1.84km), which are different from the seasonal patterns in CBH at other mid-latitude sites (maximum/minimum values in summer/winter). This may be related to different meteorological conditions as well as the analytical samplings. The seasonal vertical distribution profiles of CBH show bimodal/triple-modal styles. Analysis of the vertical

Optics EXPRESS

distribution of CBH suggests that the dominant cloud types are connective clouds and cirrus in spring and summer, stratus and altocumulus clouds in autumn and stratiform clouds in winter. The cloud is slightly thicker in winter (1.05 ± 0.43km) than in summer (0.99 ± 0.44km). This is consistent with the previous findings at other mid-latitude sites. The locations of CBH and the distribution of CGT have essential effects on the thermodynamic structure of the atmosphere and radiation budget of Earth's climate system. CF varies significantly throughout year, with the maximum value in autumn (0.68) and a minimum (0.58) in winter. CF is dominated by single-layered system (81%). The vertical distributions of CF are bimodal, with a low peak between 1 and 3 km and a high one between 7 and 8 km. More clouds are detected at night than during the day, which is important for understanding or simulating the diurnal variation of the surface energy balance.

Though the modified algorithm has good performance, there are still some deficiencies in this work. First, the lidar ratio is hypothetical, which can cause some errors in classifying atmospheric particle layers. In the future work, the other ground-based observation equipment is needed to combine with lidar to retrieve more accurate optical properties of particle layers and classify the ice cloud as randomly oriented ice (ROI) and horizontal oriented ice (HOI) further. Second, the only one year MPL data is applied in this work, which may not represent the cloud climatology sufficiently at arid and semi-arid area. The first combined Lidar-Radar cloud mask at SACOL will be established to provide more important information for studying and understanding aerosol-cloud-climate interaction and more accurate parameters for improving the simulating ability of the numerical model.

Funding

National Natural Science Foundation of China (41430425, 41505011, 41521004, 41627807); Fundamental Research Funds for the Central Universities (lzujbky-2017-58, lzujbky-2017-k03, lzujbky-2017-kb02); China 111 project (no. B13045)

Acknowledgments

The authors would like to acknowledge SACOL team for supporting the lidar data. The ECMWF team are thanked for the provision of ERA-Interim data used in this study. We would also like to thank all anonymous reviewers for their constructive and insightful comments.